Title

Safe-by-Design CuO Nanoparticles via Fe-Doping, Cu–O Bond Length Variation, and Biological Assessment in Cells and Zebrafish Embryos

Journal

ACS Nano, 11(1)

ISSN

1936-0851

Authors

Naatz, Hendrik
Lin, Sijie
Li, Ruibin
et al.

Publication Date

2017-01-24

DOI

10.1021/acsnano.6b06495

Peer reviewed

HHS Public Access

Author manuscript

ACS Nano. Author manuscript; available in PMC 2018 February 23.

Published in final edited form as:

ACS Nano. 2017 January 24; 11(1): 501–515. doi:10.1021/acsnano.6b06495.

Safe-by-Design of CuO Nanoparticles *via* Fe-Doping, Cu-O Bond Lengths Variation, and Biological Assessment in Cells and Zebrafish Embryos

Hendrik Naatz[1], **Sijie Lin**[2,3], **Ruibin Li**[4,5], **Wen Jiang**[2], **Zhaoxia Ji**[2], **Chong Hyun Chang**[2], **Jan Köser**[6], **Jorg Thöming**[6], **Tian Xia**[2,4], **Andre E. Nel**[2,4], **Lutz Mädler**[1], and **Suman Pokhrel**[1,*]

[1]Foundation Institute of Materials Science (IWT), Department of Production Engineering, University of Bremen, Germany

[2]California NanoSystems Institute, University of California, Los Angeles, California

[3]College of Environmental Science and Engineering, State Key Laboratory of Pollution Control and Resource Reuse, Tongji University, Shanghai China

[4]Division of NanoMedicine, Department of Medicine, University of California, Los Angeles, California

[5]School of Radiation Medicine and Protection & School for Radiological and Interdisciplinary Sciences (RAD-X), Medical College of Soochow University, Suzhou, Jiangsu 215123, China

[6]Centre for Environmental Research and Sustainable Technology, University of Bremen, Germany

Abstract

The safe implementation of nanotechnology requires nanomaterial hazard assessment in accordance with the material physicochemical properties that trigger the injury response at the nano/bio interface. Since CuO nanoparticles (NPs) are widely used industrially and their dissolution properties play a major role in hazard potential, we hypothesized that tighter bonding of Cu to Fe by particle doping could constitute a safer-by-design approach through decreased dissolution. Accordingly, we designed a combinatorial library in which CuO was doped with 1–10% Fe in a flame spray pyrolysis (FSP) reactor. The morphology and structural properties were determined by XRD, BET, Raman spectroscopy, HRTEM, EFTEM and EELS, which demonstrated a significant reduction in the apical Cu-O bond length while simultaneously increasing the planar bond length (Jahn-Teller distortion). Hazard screening was performed in tissue culture cell lines and zebrafish embryos to discern the change in the hazardous effects of doped *vs*. non-doped particles. This demonstrated that with increased levels of doping, there was a progressive decrease in cytotoxicity in BEAS-2B and THP-1 cells, as well as an incremental decrease in the rate of hatching interference in zebrafish embryos. The dissolution profiles were

Corresponding author: Dr. Suman Pokhrel, Foundation Institute of Materials Science (IWT), Department of Production Engineering, University of Bremen, Phone: ++49 (0)421 218-51218, Fax: ++49 (0)421 218 -98-51218, spokhrel@iwt.uni-bremen.de.

Supporting Information

The results of the Rietveld fittings of the XRD patterns, EDX interpretation, the XRD patterns of 33%Fe doped CuO and $CuFe_2O_4$, Raman spectrum, the results of cyclic voltammetry (pure FTO, pure CuO with increasing sodium bicarbonate concentration, pure CuO with change in pH, and pure Fe_3O_4) and the flow cytometry analysis of the apoptotic effects of 50 ppm 0–10% Fe doped CuO and $CuCl_2$ in BEAS-2B and THP-1 cells are available free of charge *via* the Internet at http://pubs.acs.org.

determined and the surface reactions taking place in Holtfreter's solution were validated using cyclic voltammetry (CV) measurements to demonstrate the Cu^{+}/Cu^{2+} and Fe^{2+}/Fe^{3+} redox species playing a major role in the dissolution process of pure and Fe doped CuO. Altogether, a safe-by-design strategy was implemented for the toxic CuO particles *via* Fe doping and has been demonstrated for their safe use in the environment.

Graphical Abstract

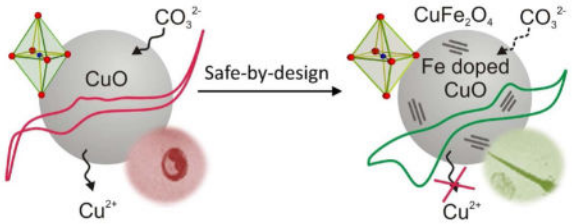

Keywords

flame spray pyrolysis; CuO nanoparticles; Fe doping; Jahn-Teller distortion; cyclic voltammetry; safe-by-design

The global consumption of copper (industrial and R&D) has more than tripled in the last 50 years and currently amounts to more than 20 million tons/year. [1–2] A large proportion of this production volume is in the form of Cu oxide, which is increasingly being used for superconducting, semiconducting, thermoelectric, sensor, ceramics, energy storage, antifouling paints, photoconductive, and photothermal applications, including in the automotive, ship, and aerospace industries. [3–14] Due to the large scale production and wide range of applications, CuO NPs are likely to come into contact with humans and the environment. [15–16] The propensity of these materials to dissolve and shed toxic copper ions has been shown to play a key role in the hazard potential of these materials. [17–24]

It is known that the cellular toxicity of CuO NPs is induced through dissolution and release of Cu^{2+}ions after their entry to the cellular interior or lysosomes. [25–26] The Cu^{2+}ions are involved in triggering series of downstream adverse effects such as ROS generation and subsequent oxidation of biological components including DNA damage. [27–29] Increased cellular uptake and the release of Cu ions disrupt metal homeostasis, trigger cell cycle progression, induce metabolic alkalosis or the production of reactive oxygen species (ROS) in the cell through the initiation of Fenton chemistry.[26, 30–35] The entry of Cu^{2+} ions and the generation of ROS in the brain causes imbalance in the oxidation/anti-oxidation process resulting into neuronal damage, learning and memory impairment.[36] The Cu^{2+} toxicity has also been observed during treatment of patients having Wilson's disease with neurological dysfunctions. The Cu-chelators used in the treatment reduce Cu^{2+} to Cu^{+} and enhance copper accumulation inducing toxicity in the brain. [37] Human exposure to CuO NPs is capable of inducing oxidative stress and acute inflammatory effects in the lungs of exposed welders, giving rise to a condition known as metal fumed fever. [38–41] Studies on zebrafish embryos also demonstrated that CuO NPs are capable of interfering in embryo hatching as a result of the inhibitory effects of released copper ions on the metalloprotease enzyme,

ZHE1, secreted by the hatching gland. [20, 24, 42–43] Moreover, the dissolution of CuO NPs has been shown to induce autophagy, which serves as a homeostatic mechanism for protecting the cell against starvation, oxidative and ER stress. [38, 44]

Against this background, we hypothesized that changing the dissolution kinetics of CuO NPs by Fe doping may present a safer nanomaterial that has a less hazardous impact by decreasing copper ion shedding. [18–20, 45–46] The expected stronger binding interaction between Cu and Fe in the particle matrix could conceptually lead to decreased particle solubility in aqueous biological environments, with the potential to reduce toxicity by a decreased dissolution. [47–48] A flame spray pyrolysis process was used for doping CuO with 1–10% Fe. The NPs were subjected to toxicological profiling in a human macrophage-like cell line (THP-1), a human bronchial epithelial cell line (BEAS-2B), and zebrafish embryos. [49–50] The cell lines represent the cell types (macrophages and epithelial cells) that serve as the 1st line of defense against inhaled NPs in the lung. Similarly, zebrafish embryos are used as a sensitive screening platform for nanomaterial toxicity in the water matrix. [20]

RESULTS

Physicochemical characterizations

The ultrafine particles obtained using versatile flame spray pyrolysis were characterized using physicochemical techniques. [49–50] The specific surface areas and BET primary particle diameters (d_{BET}) of pure and Fe doped CuO NPs were in the range from 77.6 (±1.8) to 93.6 (±4.5) m^2/g and 10–12 nm, respectively. Iron doping had very less influence on particle size.

The crystallite sizes extracted from Rietveld refinement of the XRD patterns are in the range of 9–12 nm (Figure S1 and Table 1), closely agreeing with the BET primary particle diameters. The Fe content in CuO after FSP was determined using energy-dispersive X-ray spectroscopy (EDX), showing 0.2, 2.2, 4.5, 6.3, 8.5 and 9% of Fe at calculated doping levels of 1, 2, 4, 6, 8 and 10% Fe [Figure 1(A) and S2]. The low resolution TEM of pure and/or Fe doped CuO NPs show spherical particles. Pure and Fe doped CuO particles are indistinguishable in morphology with primary particle sizes in the range of 10–20 nm. The crystalline nature of these particles is evident from high resolution images with distinct hexagonal arrangements of the octahedra [Figure 1(B) insets]. The crystal structure of the NPs was studied by probing a single particle with HRTEM imaging. The middle and lower columns in Figure 1(B) show single crystalline particles of pure and/or Fe doped CuO with well-developed lattice fringes. The lattice plane distances of 0.2529 (±0.003), 0.2514 (±0.003), 0.2308 (±0.003), 0.2323 (±0.003), 0.2528 (±0.003), 0.2518 (±0.003) and 0.2545 (±0.003) nm were observed for pure, 1, 2, 4, 6, 8 and 10% Fe doped CuO, respectively. According to these data, 2 and 4% Fe doped CuO NPs have lattice distances of ~0.23 nm while the other particles have ~0.25 nm.

The XRD patterns and the Rietveld refinement of as-prepared CuO NPs show sharp and well resolved reflections, indicating a monoclinic system (ICSD 69757) with $a = 0.46927$ nm, $b = 3.4283$ nm, $c = 5.1370$ nm, $\alpha = \gamma = 90°$, $\beta = 99.546°$. Increasing Fe loading, results in an increasing peak shift indicating Fe incorporation into the CuO lattice [Figure 2(A)]. A peak

shift of 0.35° is observed for 10% Fe doped CuO across the entire 2θ angles. At 63.62° a minor second phase (< 5% intensity) appears for ≥ 6% Fe doped CuO which agreed with the pure $CuFe_2O_4$(Figure S3).

The postulation of Fe incorporation is based on the following findings: (1) the *a* parameter of the CuO unit cell consistently increases while *b* and *c* parameters decrease with increasing Fe doping [Figure 2(B) and Figure S4] with a linear trend, agreeing with Vegard's rule [51]; (2) CuO has a square planar geometry with each Cu coordinated to 4 oxygen atoms. [52–53] The ionic radii of Cu^{2+} in square planar geometry is 0.71 Å, making it unlikely that Cu^{2+} can be substituted with Fe^{2+} having much larger ionic radii (0.77Å). However, Fe^{3+} with lower ionic radii (0.63Å) could be incorporated in the CuO lattice. [54] The structural analyses of Fe doped CuO NPs show an increase in the planar Cu-O bond length from non-doped to 2% Fe doped CuO. For iron loading of more than 2%, such increase in the bond length is only marginal. Looking at the apical Cu-O bond lengths, the result is just the reverse to the planar Cu-O indicating strong structural distortion (Jahn-Teller effect) through Fe incorporation [Figure 3(A)]. [55–56] This observation is also supported by the linear increase and decrease of a and b parameters of the CuO unit cells after Fe doping [Figure 2(B)].

Using energy filtered transmission electron microscopy (EFTEM), the results of elemental mapping of the Fe and Cu appeared to be homogeneously distributed throughout the nanoparticles at all Fe loadings [Figure 3(B)].

The room temperature Raman spectrum of reference CuO shows three signals at 291, 340 and 624 cm^{-1}, respectively. [59] With the reference to the pure CuO signals, the 291 cm^{-1} peak of our 10% Fe doped CuO was found to shift by 17 cm^{-1} towards lower frequencies due to Fe incorporation [Figure 4(A), Figure S5]. Similarly, the characteristic signal of CuO at 340 cm^{-1} becomes progressively weaker and almost undetectable at 10% Fe, while new signals appear at 442, 514, 685, 813 and 926 cm^{-1}. The intensity of these peaks is relatively constant except for the signals at 813 cm^{-1} and 926 cm^{-1} which consistently increase with increasing Fe doping [Figure 4(B)]. For higher Fe content, the characteristic Raman signal of CuO at 291 cm^{-1} occurs at a lower Raman shift resulting from the increased structural disorder closely agreeing with the XRD analyses [Figure 2(A)]. Xu *et al.* demonstrated that with a decrease in particle size, the Raman peaks shift toward lower wavenumber and *vice versa*. [60] Furthermore, Chapelle *et al.* reported Raman signal at 808 cm^{-1} for $CuFe_2O_4$ arising from ν(Cu-Fe-O). [61] The Raman signal (increasing intensity) observed for the doped particles at 813 cm^{-1} is also assigned to ν(Cu-Fe-O), a clear indication of $CuFe_2O_4$with increasing iron doping.

The oxidation states of Fe (Fe^{2+} or Fe^{3+}) in Fe doped CuO were determined using EELS spectroscopy since multiple oxidation states and coordination modes might be present in Fe doped particles. Materials containing Fe^{2+} or Fe^{3+} are most commonly octahedral-coordinated although tetrahedral coordination of Fe is also known. Usually Fe is expected to be in the high-spin state with strong field ligands causing spin pairing. Fe $L_{2,3}$ edges acquired from a number of reference materials containing Fe^{2+} and Fe^{3+} in both octahedral and tetrahedral coordination [chromite (Fe^{2+}), siderite (Fe^{2+}) hematite (Fe^{3+}) and leucite (Fe^{3+})] show different edge shapes, as well as a distinct chemical shift between the divalent

and trivalent oxidation states [Figure 4(C)]. [57–58, 62] The L_3 edges for the divalent Fe minerals are ~ at 706.4 eV, and the trivalent Fe L_3 edge is 1.7 eV higher at 708.1 eV. The separation of the L_3 and L_2 peak maxima, due to spin orbit splitting is ~13 eV. The EELS spectra of 1%, 4% and 10% Fe doped CuO show Fe L_3 edges occurring at 708.8 eV (d-d transitions of d electrons into the unoccupied 3d-states) agreeing with the trivalent Fe of hematite (Fe^{3+}) and/or leucite (Fe^{3+}) [Figure 4(D)]. [57–58, 62] The spin orbit coupling constant for the Fe doped CuO NPs was found to be 13.1 eV as for hematite and/or leucite [Figure 4(C) and (D)]. [63–64] The presence of Fe^{3+} is a clear indication of the stabilized Cu–Fe–O phase [65] on the CuO nanoparticle surface which prevents dissolution when these particles are exposed to the cellular medium.

Characterization of CuO dispersions and dissolution properties

Hydrodynamic sizes of pure and/or Fe doped CuO NPs were found to be in the range of ~210–434, ~225–457, ~349–664 and ~366–638 nm in DI water, Holtfreter's Medium, RPMI 1640 medium and BEGM medium respectively. The zeta potential measurements in DI water (at pH ~ 6.5–7.4) indicate that 2–6% Fe doped CuO have surface positive charges while 8% and 10% Fe doped CuO have negative surface charges. A measurement of the pure $CuFe_2O_4$ NPs showed a zeta potential of −19.6±1.8 mV in DI water, which agrees with the data reported in the literature. [66–67] The negative surface charge of 8% and 10% of iron in CuO is due to increasing $CuFe_2O_4$ on the surface, which is evidenced through cyclic voltammetry (CV) discussed in the next section. NP dispersion in Holtfreter's medium, RPMI 1640 medium and BEGM medium (at pH ~7.6–7.8), resulted in the negative surface charge of the particles, ranging from −8.5±2.9 to −23.16±5.8 mV, which is likely caused by serum albumin in RPMI 1640 medium and alginate that is used as a dispersing agent in Holtfreter's medium (Table 1). [19–20] Clear differences in the NP dissolution profiles in Holtfreter's medium, DI water, and the various cell culture media are shown in Figure 5. While Fe doping generally decreases the amount of dissolved ions, the concentrations were much higher in cell culture compared to Holtfreter's medium. The dissolved ion concentration in DI water was much lower and almost insignificant compared to Holtfreter's or the cell culture media [see Figure 5(A) and (B)].

Cyclic voltammetry of pure and Fe doped CuO NPs

The cyclic voltammetry (CV) experiments were conducted in the Holtfreter's medium for all the samples [Figures 6 and 7(A)–(D)]. The results of the pure CuO showed two anodic signals (A_1 and A_2) occurring at −150 mV and 100 mV, respectively, assigned to redox processes on the CuO surface [Figure 6]. The FTO glass (used as a conducting substrate coated with CuO particles [inset of Figure 6]) itself does not interfere in the Holtfreter's medium [Figure S6(A)].

The interaction of the carbonate species in Holtfreter's medium with the CuO NPs surface was demonstrated by varying the $NaHCO_3$ concentration (2.4 mM to 36 mM in the Holtfreter's medium). The A_1 signal intensity at 36 mM $NaHCO_3$ is much larger compared to the signal intensity at 2.4 mM $NaHCO_3$(oxidation reaction involving CO_3^{2-}), while the respective reduction signal C_1 occurs at −200 mV [Figure S6(B)]. The oxidation reaction (A_1) clearly demonstrates the interaction of the CuO particles with the carbonate species.

This interaction results in a change in pH, which might be responsible for the dissolution of CuO. [68] The second oxidation signal (A_2) is likely due to Cu^{+}/Cu^{2+} redox couple triggered through the formation of Cu_2O (reduction of CuO) in the negative slope below −400 mV. [69–70] The negative potential is too low for a complete reduction (limited by the electrochemical window of the FTO glass) and hence, the A_2 signal vanished with increasing number of cycles (Figure 6). At potentials above 400 mV, further oxidation of the CuO occurs in the anodic slope (A_3) with the corresponding reduction signal (C_3) at similar potentials. Both processes are influenced by the change in pH, indicating the role of OH^{-}in the redox reaction [Figure S6(C)].

The results of the cyclic voltammetry of the Fe doped CuO NPs showed two additional redox signals $A_{CuFe2O4}$ and $C_{CuFe2O4}$ [overlapping with C_1, see Figure 7(A)–(D)]. These signals were observed at the potential of 200 mV and −200 mV (oxidation and reduction) due to surface reaction with the spinel $CuFe_2O_4$.[71] Both signals are clearly visible for the 6–10% Fe doped CuO NPs [Figure 7(A) and (C)]. To demonstrate the presence of this phase ($CuFe_2O_4$), a new material with high Fe loading (33%) was synthesized with the flame spray pyrolysis. The redox signals of 33% Fe added CuO NPs showed enhanced $A_{CuFe2O4}$ and $C_{CuFe2O4}$ signal intensities clearly indicating the presence of the $CuFe_2O_4$ that is corroborated by the characteristic XRD peak of $CuFe_2O_4$ occurring at (62° 2θ) [Figure 7(B) and S3]. While the first anodic scans from 0 to 600 mV vs. Ag/AgCl for all the particles tested had no spinel oxidation signal, it appeared only after reducing at a sufficiently negative potential in the subsequent scans indicating the presence of $CuFe_2O_4$ prior to CV cycling. The emerging A_{Fe} signal was attributed to Fe^{2+}/Fe^{3+} redox couple where the intensity increased with increasing Fe [Figure 7(C) and (B)]. To exclude that the Fe^{2+}/Fe^{3+} redox couple is from Fe_3O_4, the cyclic voltammetry experiments were conducted for pure Fe_3O_4. In these experiments, the A_{Fe} signal was not detected [Figure S6(D)]. The quasi-stationary 30^{th} cycle were recorded with a higher scan rate at 100 mVs^{-1} to enhance the spinel $A_{CuFe2O4}$ and $C_{CuFe2O4}$ signals [Figure 7(D)].

While the spinel oxidation signals were only visible after 4% Fe doping, the signal resulting from the copper oxidation involving carbonate was found to decrease and vanish completely for more than 6% Fe loading. The results indicate the inhibition of the reaction involving CO_3^{2-} is due to the presence of $CuFe_2O_4$ (reduced dissolution) [Figure 5(A)]. In addition, the oxidation process in the anodic region which might contribute to the dissolution of the CuO NPs, is shifted to higher potentials with increase in Fe content suggesting dissolution hindrance due to doping. [69]

Cytotoxicity, autophagy and embryo hatching

Previous studies demonstrated that the intra and extracellular dissolution of CuO particles is responsible for biological outcomes such as cytotoxicity and autophagy. [24, 31, 72] We asked, therefore, whether a change in nanoparticle dissolution characteristics of the NPs could impact these responses in mammalian cells.

To test the hypothesis, the bioresponse of pure and doped CuO NPs were assessed in THP-1 and BEAS-2B cells (representative of the responses for macrophages and bronchial epithelial lung cells). [19] While non-doped CuO NPs induced dose-dependent cytotoxicity in

BEAS-2B cells, iron doping resulted in a significant reduction in cell death [Figure 8(A) and (B)]. This protective effect was incremental with the level of doping, such that doping at >6% resulted in the abrogation of cell death at a particle concentration of 100 μg/mL. However, a physical mixture of CuO and 10% Fe_3O_4 NPs showed similar biological response (extent of cell death) compared to non-doped particles [Figure 8(A) and (B)] clearly suggesting the efficient doping effect during flame spray pyrolysis. This indicates that the doping rather than physical mixture plays a key role in reducing CuO cytotoxicity. Albeit less prominent, iron doping resulted in similar protective effects in THP-1 cells [Figure 8(C)–(D)]. In addition, the cell death was minimal when the same concentration of $CuCl_2$ salt was exposed to the cellular system studied compared to the CuO NPs [Figure 8(B) and (D)] reasonably agreeing with the literature. [25, 73]

The effects of Fe doping on autophagy, a stress-induced homeostatic response was also studied using the autophagosome assembly marker, LC-3II, which can be visualized by confocal microscopy in THP-1 cells that are stained with FITC-labeled anti-LC-3II antibodies. [40] As shown in Figure 9, non-doped CuO NPs induced autophagosome formation, which was significantly less prominent in cells treated with 10% Fe doped CuO NPs. Chloroquin (CQ) was used as a positive control. The quantification of cellular content of Cu and Fe in BEAS-2B and THP-1 cell lines exposed to 50 ppm of 0–10% Fe doped CuO after 24 h using ICP-OES showed increased cellular Cu and Fe uptake with the increase in Fe doping [see Figure 10(A)–(E)]. The similar experiment using copper salt ($CuCl_2$) showed no Cu^{2+} uptake. Flow cytometric analysis (early and late cellular apoptosis/necrosis) was used to study the apoptotic effects of 50 ppm 0–10% Fe doped CuO and $CuCl_2$ in BEAS-2B cells at 24 h by using Annexin V-FITC and propidium iodide (PI) double-labeling technique (see Figure S7). Results showed doping effectively reduced early and late apoptosis as well as increased live BEAS-2B cells. Similarly, flow cytometric analysis of the apoptotic effects at 50 ppm of 1–10% Fe doped CuO and $CuCl_2$ in THP-1 cells also indicated reduced early and late apoptosis/necrosis (see Figure S8). Despite higher cellular uptake of Fe-doped CuO, there were no increase in the cell death; on the contrary, the cell death decreased as the doping percentage increases. This strongly suggests that reduced particle dissolution by Fe doped CuO decreased CuO-induced cytotoxicity. Taken together, iron doping could greatly reduce the cell death as well as autophagosome accumulation.

Furthermore, results showed ~50% late apoptosis and 25% early apoptosis induction *via* pure CuO exposure in BEAS-2B cells, while 1%–10% Fe doped CuO induced less than 40% late apoptosis and 10 % early apoptosis [see Figure 10(D)]. The percentage of live cells increased from 25% for CuO to more than 60% for 10% Fe doped CuO. THP-1 cells showed similar results as BEAS-2B cells, especially for the effects onearly apoptosis [see Figure 10(E)].

It was previously demonstrated that ionic dissolution of specific transition metal oxide NPs, including CuO, can interfere in embryo hatching due to an effect on the metalloprotease hatching enzyme, ZHE1.[19–20] Figure 11(A) and (B) show the effects of pure and doped NPs on embryo hatching. The data clearly show the reduction of the hatching interferences through Fe doping at low concentrations [Figure 11(B)].

DISCUSSION

Almost a decade ago, Karlsson *et al.* reported cellular toxicity of CuO NPs *via* dissolution. They observed Cu^{2+} released from CuO NPs were much more toxic than Cu^{2+} ions from $CuCl_2$ salt. [25, 73] The CuO NPs passing through the cell membrane penetrate lysosomes and release Cu^{2+} ions *via* Trojan-horse mechanism. [26] Similarly, two systematic studies on CuO dissolution and the involvement of Cu^{2+} in triggering series of adverse effects on algal growth showed Cu^{2+} shedding a key factor for toxicity induction. [27, 74] They suggested Cu^{2+} internalization generates ROS which activates superoxide dismutase gene for unspecific oxidation of various biomolecules including DNA. The simultaneous determination of ROS, NP uptake and their correlation with genotoxicity after exposing the cells with various nanoparticles such as ZnO, CuO, Fe_3O_4, TiO_2, and Ag showed the former two (ZnO and CuO) produced high ROS triggering phosphorylated histone γ-H2AX, a signal for DNA damage. [28–29] The toxicity of CuO NPs on the cognitive functions of rats caused learning and memory impairment due to imbalance of oxidation/anti-oxidation homeostasis. [36] In addition, Cu^{2+} ions are known to regulate genes associated with Mitogen-Activated Protein Kinase (MAPK) pathway, cell cycle progression, DNA damage human lung cells apoptosis indicating the role of Cu^{2+} in adverse biological responses. [38, 73, 75] The most significant toxic result was observed during the stabilization of neurological functions in the patients with Wilson's disease when excess copper was chelated. These Cu-chelators were found to reduce Cu^{2+} to Cu^{+} and enhance copper accumulation as well as induce brain cells toxicity. They suggested the attempts of rescuing brain cells against copper-induced ROS exploiting Cu-chelators are highly risky. [37] In very recent reports, Hedberg *et al.* showed cellular membrane damage due to NP corrosion which helped accelerate dissolution. [76] In addition, the dissolution of CuO NPs caused specific developmental effects in sea urchin embryos due to disruption in the aboral-oral axis related to altered gene expression induced by changes in the redox environment. [43] Similar to these investigations, the flame sprayed CuO NPs in the present investigation were found to be toxic to THP-1 and BEAS-2B cells as well as hatching interference in zebrafish embryos. While extensive use of CuO based NPs in the industry and R&D world-wide is a clear indication for the potential exposure of the particles, there is an urgent need to re-design CuO NPs to increase safety margin when these aerosol CuO NPs are deliberately/undeliberately exposed to the environment. Hence, the CuO nanoparticles were doped with Fe to reduce the dissolution and to increase such safety margin.

Safe-by-designed CuO based nanoparticles

The CuO NPs were doped using in-house build flame spray pyrolysis (FSP), a key synthesis process to re-engineer CuO NPs at elevated temperatures. The Fe doping at such high temperatures in symmetrical CuO results in structural distortion producing stable material (Jahn-Teller effect). [77,78] The XRD analysis of the Fe doped CuO shows inward movement of the trans oxygen ligands by 2.19 Å for pure CuO and 2.05 Å for 10% Fe doped CuO while the planar oxygen ligands moves outward with 2.02 Å for pure CuO and 2.19 Å for 10% Fe doped CuO making almost 6.4% of plane elongation and apparent distortion of 4.1% (Figure 3). Such lattice distortion explains the material stability due to the formation of $CuFe_2O_4$on the surface. [65]

The exposure of these pure and Fe doped particles in test models (THP-1 and BEAS cells as well as zebrafish embryos) showed reduced Cu^{2+} release from the doped particles and almost no release for 10% Fe doped CuO NPs. The dissolution of the CuO NPs in Holtfreter's medium is likely triggered by a redox reaction taking place on the CuO surface in presence of sodium bicarbonate. Hence, the use of bicarbonate species as an electron acceptor in the biological medium triggers increased pH and enhances further dissolution.[68] The reduced dissolution of Fe doped CuO is due to the formation of a stable $CuFe_2O_4$ phase at the surface of the Fe doped CuO NPs. The insoluble $CuFe_2O_4$ (supported by our extensive physicochemical characterizations and the cyclic voltammetry, Figure 6 and 7) on the Fe doped CuO prevents Cu^{2+} release in the cellular interior. [79–80] While the redox signals only appeared after reducing the spinel, it is obvious that the spinel is already present.

The biological response assessment in THP-1 and BEAS-2B cells, showed dose-dependent cytotoxicity for CuO NPs, while CuO NPs with >6% Fe had protective effects even at the highest dose (100 μg/mL) [Figure 6(A) and (B)]. Similarly exposure of CuO based library in zebrafish embryos clearly showed the reduction of the hatching interferences with respect to Fe doping. The striking observation is that the physical mixture of CuO and 10% Fe_3O_4 showed no decrease in apoptosis compared to pure CuO NPs confirmed acquiring autophagy response for 10% Fe doped CuO. Hence, pure CuO NPs were toxic to all the test models and the reduced dissolution (increased formation of $CuFe_2O_4$ spinel) *via* Fe doping was proportional to the reduction in toxicity and/or hatching interference clearly indicating the importance of safe designed CuO particles before they can be released in the environment(Figure 12).

The dissolution driven cytotoxicity of pure ZnO in cell models, zebrafish, rat, mouse (using high throughput system) and variety of organisms at different trophic levels in the environment, including bacteria, algae, crustaceans, ciliates, yeast, fish, and nematodes was previously demonstrated. [23, 46, 81–83] The biological response was then delineated by engineering ZnO NPs *via* Fe doping. [46, 84–86] In the present investigation, the decreased toxicity at cellular level and the reduced hatching interference in the zebrafish embryo (safe-by-design strategy) is established for Fe doped CuO NPs (Figure 12). The role of physicochemical properties of pure and Fe doped CuO playing a decisive part in NP toxicity (particle dissolution and Cu^{2+} release) is demonstrated. Although Fe doping was considered to be a key strategy to reduce ZnO toxicity in the environment,[46, 87] there are major differences in the toxicity reduction mechanism between Fe doped CuO and/or ZnO. In the case of Fe doped CuO NPs, the Fe incorporation has two effects: (1) stabilizes the CuO crystal lattice through distortion (4.1% when 10% Fe is doped in CuO) Considering d^9 configuration for CuO, Cu^{2+} finds itself in the center of the six octahedral oxygen ligands (2 in the apical positon and 4 in the planar position) [see Figure 3(A)]. When Fe is doped in CuO, one of the *d* sub-orbitals of Cu is vacant making the electronic states of e_g orbital degenerate, resulting in a Jahn-Teller distortion. [77–78] (2) formation of surface $CuFe_2O_4$ spinel (only detectable for higher Fe loading). The stable material and increasing surface $CuFe_2O_4$ spinel with increase in doping prevents excess Cu^{2+} release to significantly mitigate the cytotoxicity. However, the stabilization in Fe doped ZnO implies Fe^{2+} to be more strongly bound than Zn^{2+} in the crystal structure. For Fe doped ZnO, the central metal Zn has d^{10} configuration and cannot undergo Jahn–Teller distortion. From the earlier

investigation, it is known that there are no detectable structural differences even after loading 10% of Fe due to the possibility of doping Fe beyond the solubility limit in the FSP process. [22] Taken all together, doping does offer a safer alternative for toxic CuO NPs when they enter the living system, but still requires careful investigation with respect to the specific application and model organisms.

CONCLUSION

In the present investigation pure and Fe doped CuO NPs homologues library has been designed using in-house built flame spray pyrolysis. The extent of dissolution has been significantly lowered by incorporating Fe in CuO NPs. Cyclic voltammetry demonstrated the formation of $CuFe_2O_4$ at the surface for Fe concentrations above 6%. With an increase in Fe doping, the oxidation reaction of sodium bicarbonate a probable cause for the CuO dissolution, is strongly reduced. The doped particle exposed to zebrafish embryos showed reduced interference of ZHE1 enzyme and enzyme activity (improved safety profiles) due to reduced dissolution. The biological response assessment in pure CuO exposed THP-1 and BEAS-2B cells showed dose-dependent cytotoxicity while CuO doped with ≥6% Fe showed protective effects even at high concentration. Altogether, the data suggested Fe doped CuO could serve as an example for extending safer-by-design rule to many other particles (posing hazard potential to the human and the environment)used in commercial applications.

METHODS

Synthesis of pure and/or Fe doped CuO NPs

Flame spray pyrolysis was used for the production of ultrafine powders of pure and/or Fe doped CuO NPs. [22, 49] The synthesis was performed using copper naphthenate (Strem Chemicals, 99.9% pure) with/without iron naphthenate (12% Fe by metal, Strem Chemicals, 99.9% pure). For Fe doping in CuO, the required amount of iron naphthenate was mixed with the copper naphthenate solution before combustion. For instance, the synthesis of 10% Fe is calculated as: %Fe = Weight of Fe in 5.7 mL of a 0.5M solution/(Weight of Fe in 5.7 mL of 0.5M solution + weight of Cu in 50 mL of a 0.5M copper naphthenate solution). All precursors were diluted with xylene (Strem Chemicals, 99.95% pure) to obtain a total metal concentration of 0.5 M. To synthesize the complete library of Fe doped CuO, a 50 mL portion of 0.5 M copper naphthenate was separately mixed with 0.57–5.7mL of 0.5 M iron naphthenate to obtain 1–10 %Fe in CuO. During synthesis, the liquid precursor was delivered to the two-phase nozzle at the rate of 5 mL/min using a syringe pump and was atomized with oxygen at flow rate of 5 L/min O_2 (pressure drop of 1.5 bar at the nozzle tip). [88] The spray was ignited with a premixed flame of CH_4 and O_2 flowing at a rate of 1.5 and 3.2 L/min, respectively. The ultrafine particles were collected from the 257 mm glass filters placed at a distance of 60 cm from the nozzle. [50, 83, 89]

X-ray diffraction (XRD) and Rietveld analysis

The in-house synthesized pure and/or Fe doped CuO NPs were placed in circular sample holders (diameter of 16 mm) and loaded in Bruker D8 diffracting system. The diffractometer was configured in Bragg-Brentano geometry equipped with a primary Johansson

monochromator producing Ni-filtered Cu-K_α (λ=0.154 nm) radiation. A 0.1° fixed divergence, 4° primary, 2.5° secondary soller slits, and LynxEye detector (position sensitive in a range of 3° 2θ with 192 channels, yielding a channel width of 0.01563° 2θ) was used. Continuous scans were applied with an integration step width of 0.03° 2θ and 30 s per step. The structural and microstructural parameters were extracted using Rietveld refinement by applying BRASS program. [90] Background, scale factor, unit cell parameters, Gaussian as well as Lorentzian peak width parameters were simultaneously refined to obtain the crystallite size. For the pattern refinement, the structural model for CuO (ICSD-69757) with monoclinic space group C1C1 [a=4.6927(4), b=3.4283(4), c=5.1370(6), β=99.546(9)] was used. The quality of Rietveld refinement was evaluated in terms of the usual R factor (R_{wp}) and the background corrected residual R'_p. [91] A volume weighted average crystallite size (d_{XRD}) and the root-mean-square lattice micro strain for each of the doped CuO samples were determined. The instrumental contribution to the peak broadening was taken into account using instrumental parameters derived from standard crystalline LaB_6.

Brunauer-Emmett-Teller (BET) measurements

BET measurements were carried out at 77K using a Quantachrome NOVA 4000e Autosorb gas sorption system to determine the specific surface areas of the samples. The powders were placed in a test cell and allowed to degas for 2 hours at 200°C in flowing nitrogen to remove water vapour and adsorbed gases from the samples. Data were obtained by exposing or removing a known quantity of adsorbing gas in or out of a sample cell containing the solid adsorbent maintained at the constant liquid nitrogen temperature. BET surface area measurement is related to the average equivalent primary particle size as $d_{BET} = 6000/(\rho \cdot S_A)$, where d_{BET} is the average diameter of the spherical particles (nm), S_A the measured specific surface area (m^2/g), and ρ is the theoretical density in g/cm^3. [49]

Transmission Microscopy (TEM) imaging

For the TEM specimen preparation, a small portions of the FSP-generated pure and/or Fe doped CuO powder (~1–2 mg) were dispersed in 5mL of ethanol (Strem Chemicals, AR grade) in an ultrasonic bath and sonicated for 15 minutes. A drop of the dispersed sample was placed on a nickel grid coated with carbon film (Cu grid was not used as it would interfere with the Cu in the sample during extraction of the quantitative elemental data). The samples were dried at RT followed by scanning the large regions of the grid. The low and high resolution TEM of the sample were examined using transmission electron microscopy (TEM) on a FEI Titan 80/300 microscope equipped with a Cs corrector for the objective lens, a Fischione high angle annular dark field detector (HAADF), GATAN post-column imaging filter and a cold field emission gun operated at 300 kV as an acceleration voltage. For the electron energy loss spectroscopy (EELS) measurement, the Gatan parallel EELS spectrometer was operated at 0.2 eV per channel as an energy dispersive detector. Imaging was performed at each sampling point in order to identify the homogeneity of the samples.[92] EFTEM images of pre and post edges of elemental mappings were obtained from the data by energy calibration and background subtraction. Zero loss and low loss spectra were also taken at each sampling point for energy calibration using the energy of the zero loss, low loss or core loss at the lower energy.

Raman measurements

The Raman spectra were collected using pressed powder samples on glass plates (~5 mm diameter). The spectra were recorded on a Horiba LabRam Aramis spectrometer equipped with a solid state Nd-YAG laser with wavelength centered at 532 nm. Data were collected by scanning the wide spot in the range of 50–2000 cm^{-1} with a spectral resolution of ~3.2 cm^{-1} using a grating of 1800 grooves/mm.

Nanoparticle dissolution studies

To determine particle dissolution in biological media, particles were dispersed at 50 ppm in cell culture medium and at 0.5 ppm in Holtfreter's medium for 0, 24 and 48 h. After vortexing of the suspensions and centrifugation at 15 000 rpm for 1 h, supernatants were transferred to clean tubes for acid digestion. Digestion was carried out with concentrated nitric acid (10 mL of HNO_3, 65–70%, Trace Metal grade) at 80 °C for 6 h in a HotBlock (SC100, Environmental Express). The temperature was increased to 95 °C to evaporate the remaining liquid. The samples were cooled to room temperature and resuspended in 2% nitric acid at 80 °C for 3 h. The resulting solutions were transferred to 15 mL ICP-OES analysis tubes and brought to a final volume of 8 mL through the addition of nitric acid. ICP-OES analysis was carried out in a Shimadzu ICPE 9000 to determine the elemental Cu concentration. A calibration curve was established using a standard Cu solution (Elements Inc., 1000 mg/L in 2% HNO_3). Each sample and standard was analyzed in triplicate in the presence of 2% (v/v) nitric acid.

Electrochemical characterization using cyclic voltammetry (CV)

The CV measurements were carried out in a three-electrode system consisting of an Ag/AgCl (3M KCl, SI Analytics) reference electrode, a Pt-coated grid as counter electrode and the working electrode. The working electrodes (8 cm^2) were prepared using double-roll laminator (Hot Roll Laminator HL-101, Cheminstruments) where the particles from FSP collecting unit were directly transferred (glass fiber filter) to the conductive FTO (fluorine doped tin oxide) glass substrates (7 Ω cm^{-2}, Sigma Aldrich). The dry particle transfer process enables crack-free coating of nanoparticle layers on the electrodes. [93] After transferring the particles with a pressure of 3.2 MPa, a subsequent heat treatment at 350 °C for 6 h stabilizes the particles on the FTO surface. The CV's were recorded with a potentiostat (IMP83, Jassile) at a scan rate of 25 and/or 100 mVs^{-1} at a fixed potential range of −600 to 600 mV vs. Ag/AgCl using Holtfreter's solution as an electrolyte. Prior to the measurements, the electrolyte was purged with N_2 for 30 minutes. The experiments were carried out at a constant temperature of 22±1°C.

Preparation of NPs in cell culture media

CuO NPs were suspended in distilled, deionized H_2O at a concentration of 5 mg/mL. A water sonicator (Branson, Danbury, CT, USA, model 2510) was used to sonicate these suspensions at 100 W output with a frequency of 42 kHz for 15 min. The suspensions were used as stock solutions for further dispersion in RPMI1640 or BEGM media. An appropriate amount of each stock solution was added to cell culture media to achieve the desired final concentration. For RPMI 1640, the media were supplemented with 10% fetal bovine serum

(FBS). For BEGM, BSA was added to the medium at 0.2 mg/mL, before the addition of CuO NPs to achieve a high dispersion. [19–20, 23–24] The diluted CuO suspensions in cell culture media were dispersed using a sonication probe (Sonics & Materials, USA) at 32 W for 15 s before exposure to the cells.

Cytotoxicity Assessment

THP- 1 and BEAS-2B cells, purchased from ATCC (Manassas, VA), were cultured in RPMI 1640 medium supplemented with 10% FBS (c-RPMI 1640 and BEGM, respectively, at 5% CO_2 and 37 °C). Before exposure to the CuO NPs, BEAS-2B cells were seeded at a density of 2×10^3/well in 96-well plates (Corning, NY, USA) at 37 °C overnight. For THP-1 cells, aliquots of 5×10^4 THP-1 cells were seeded in 0.1 mL c-RPMI 1640 medium with 1 μg/mL phorbol 12- myristate acetate (PMA) overnight in 96-well plates (Corning, NY, USA). All the CuO suspensions were freshly prepared in BEGM with 0.2 mg/mL BSA or c-RPMI 1640 before addition to the BEAS-2B and THP-1 cells (120 μL/well), respectively. After 24 h treatment, the cell culture medium was removed by aspiration. Each well received 100 μL of culture medium containing 16.7% of MTS stock solution for 1 h at 37 °C. The plate was centrifuged at 3000 g for 5 min in NI Eppendorf 5430 with a microplate rotor to spin down the cell debris. A 100 μL amount of the supernatant was transferred into a new plate. The absorbance of formazan in culture media was read at 490 nm on a SpectraMax M5 microplate reader (Molecular Devices Corp., Sunnyvale, CA, USA).

Confocal imaging of autophagosomes

BEAS-2B cells were seeded in a 8-well chamber slide at $2\times10^{4/}$well. After exposure to pure or Fe doped CuO NPs at 25 μg/mL for 24 h, the cells were fixed in 4% paraformaldehyde for 30 min and permeabilized by 0.2% Triton X-100 for 15 min. Permeabilized cells were subsequently incubated with primary LC-3II antibodies at 4 °C overnight, followed by washing and the addition of secondary antibody or Hoechst for 2 h at room temperature. [40] After washing, the cells were visualized under a confocal microscope (Leica Confocal SP2 1P/FCS) in the UCLA/CNSI Advanced Light Microscopy/Spectroscopy Shared Facility. High magnification images were obtained with the 63 X objective.

Zebrafish embryo nanoparticle exposure

Wild type adult zebrafish (Danio rerio) were housed and maintained in the UCLA zebrafish facility. Two pairs of male/female fish were placed in a single tank one day ahead of time and released the next morning to trigger spawning. The embryos were collected at 2 hour post fertilization (hpf) and rinsed with Holtfreter's medium to remove any residue from the embryo surface. Subsequently, fertilized embryos were robotically pick-and-placed into 96-well plates with one embryo in each well. Exposure started at 4 hpf by adding 100 μL of the nanoparticle suspension into each well of the multitier plates. Twelve replicates for each treatment group were used to allow statistical analysis. The hatching rate and survival percentage were assessed at day 3 of embryo development and used as toxicity endpoints. Bright-field high content imaging (ImageXpress) was performed to capture high resolution microscopic images of embryos as previously described. [19–20] All procedures were carried out in accordance with the Animal Care and Use Committee guidelines at UCLA.

Supplementary Material

Refer to Web version on PubMed Central for supplementary material.

Acknowledgments

Primary support was provided by the US Public Health Service Grant, RO1 ES016746. The work also leveraged the infrastructure that is supported by the National Science Foundation and the Environmental Protection Agency under Cooperative Agreement Number DBI 0830117 and 1266377. J.K and J.T would like to gratefully acknowledge the support from the Federal Ministry of Education and Research (BMBF, support code 03X0152). S.P. and L.M. would like to thank Prof. A. Rosenauer, Department of Solid State Physics, for the TEM imaging of the dry powder.

References

1. [accessed 27.10.2016] DaNa $^{2.0}$ Copper and Copper Oxides - Overview. http://www.nanopartikel.info/en/nanoinfo/materials/copper-and-copper-oxides
2. International Copper Study Group. Copper Bulletin. International Copper Study Group; Lisbon, Portugal: 2012.
3. Ahn JY, Kim WD, Kim JH, Kim JH, Lee JK, Kim JM, Kim SH. Gas-Phase Synthesis of Bimetallic Oxide Nanoparticles with Designed Elemental Compositions for Controlling the Explosive Reactivity of Nanoenergetic Materials. J Nanomater. 2011; 2011:7.
4. Chen H, Leng W, Xu Y. Enhanced Visible-Light Photoactivity of $CuWO_4$ Through a Surface-Deposited CuO. J Phys Chem C. 2014; 118:9982–9989.
5. Duan Y, Liu X, Han L, Asahina S, Xu D, Cao Y, Yao Y, Che S. Optically Active Chiral CuO "Nanoflowers". J Am Chem Soc. 2014; 136:7193–7196. [PubMed: 24802633]
6. He Z, Lin C, Cheng W, Okazawa A, Kojima N, Yamaura J-i, Ueda Y. Unusually Large Magnetic Anisotropy in a CuO-Based Semiconductor $Cu_5V_2O_{10}$. J Am Chem Soc. 2011; 133:1298–1300. [PubMed: 21192711]
7. Hosseini SG, Abazari R. A Facile One-Step Route for Production of CuO, NiO, and CuO-NiO Nanoparticles and Comparison of Their Catalytic Activity for Ammonium Perchlorate Decomposition. RSC Adv. 2015; 5:96777–96784.
8. Hübner M, Simion CE, Tomescu-Stănoiu A, Pokhrel S, Bârsan N, Weimar U. Influence of Humidity on CO Sensing with P-Type CuO Thick Film Gas Sensors. Sens Actuators, B. 2011; 153:347–353.
9. Lu Y, Liu X, Qiu K, Cheng J, Wang W, Yan H, Tang C, Kim JK, Luo Y. Facile Synthesis of Graphene-Like Copper Oxide Nanofilms with Enhanced Electrochemical and Photocatalytic Properties in Energy and Environmental Applications. ACS App Mater Interfaces. 2015; 7:9682–9690.
10. Sahay R, Suresh Kumar P, Aravin dan V, Sundaramurthy J, Chui Ling W, Mhaisalkar SG, Ramakrishna S, Madhavi S. High Aspect Ratio Electrospun CuO Nanofibers as Anode Material for Lithium-Ion Batteries with Superior Cycleability. J Phys Chem C. 2012; 116:18087–18092.
11. Schmidt R, Sinclair DC. Anomalous Increase of Dielectric Permittivity in Sr-Doped CCTO Ceramics $Ca_{1-x}Sr_xCu_3Ti_4O_{12}$($0 \le x \le 0.2$). Chem Mater. 2010; 22:6–8.
12. Wei T, Huang YH, Zhang Q, Yuan LX, Yang JY, Sun YM, Hu XL, Zhang WX, Goodenough JB. Thermoelectric Solid-Oxide Fuel Cells with Extra Power Conversion from Waste Heat. Chem Mater. 2012; 24:1401–1403.
13. Yan S, Jian G, Zachariah MR. Electrospun Nanofiber-Based Thermite Textiles and Their Reactive Properties. ACS App Mater Interfaces. 2012; 4:6432–6435.
14. Zhao Y, Torres P, Tang X, Norby P, Grivel JC. Growth of Highly Epitaxial $YBa_2Cu_3O_{7-\delta}$ Films from a Simple Propionate-Based Solution. Inorg Chem. 2015; 54:10232–10238. [PubMed: 26473556]
15. Fu PP, Xia Q, Hwang HM, Ray PC, Yu H. Mechanisms of Nanotoxicity: Generation of Reactive Oxygen Species. J Food Drug Anal. 2014; 22:64–75. [PubMed: 24673904]
16. Nowack B, Bucheli TD. Occurrence, Behavior and Effects of Nanoparticles in the Environment. Environ Pollut. 2007; 150:5–22. [PubMed: 17658673]

17. Kaweeteerawat C, Ivask A, Liu R, Zhang H, Chang CH, Low-Kam C, Fischer H, Ji Z, Pokhrel S, Cohen Y, Telesca D, Zink J, Mädler L, Holden PA, Nel A, Godwin H. Toxicity of Metal Oxide Nanoparticles in *Escherichia coli* Correlates with Conduction Band and Hydration Energies. Environ Sci Technol. 2015; 49:1105–1112. [PubMed: 25563693]
18. Li M, Pokhrel S, Jin X, Mädler L, Damoiseaux R, Hoek EMV. Stability, Bioavailability, and Bacterial Toxicity of ZnO and Iron-Doped ZnO Nanoparticles in Aquatic Media. Environ Sci Technol. 2011; 45:755–761. [PubMed: 21133426]
19. Lin S, Zhao Y, Ji Z, Ear J, Chang CH, Zhang H, Low-Kam C, Yamada K, Meng H, Wang X, Liu R, Pokhrel S, Mädler L, Damoiseaux R, Xia T, Godwin HA, Lin S, Nel AE. Zebrafish High-Throughput Screening to Study the Impact of Dissolvable Metal Oxide Nanoparticles on the Hatching Enzyme, ZHE1. Small. 2013; 9:1776–1785. [PubMed: 23180726]
20. Lin S, Zhao Y, Xia T, Meng H, Ji Z, Liu R, George S, Xiong S, Wang X, Zhang H, Pokhrel S, Mädler L, Damoiseaux R, Lin S, Nel AE. High Content Screening in Zebrafish Speeds up Hazard Ranking of Transition Metal Oxide Nanoparticles. ACS Nano. 2011; 5:7284–7295. [PubMed: 21851096]
21. Nel AE, Mädler L, Velegol D, Xia T, Hoek EMV, Somasundaran P, Klaessig F, Castranova V, Thompson M. Understanding Biophysicochemical Interactions at the Nano-Bio Interface. Nat Mater. 2009; 8:543–557. [PubMed: 19525947]
22. Pokhrel S, Nel AE, Mädler L. Custom-Designed Nanomaterial Libraries for Testing Metal Oxide Toxicity. Acc Chem Res. 2013; 46:632–641. [PubMed: 23194152]
23. Xia T, Zhao Y, Sager T, George S, Pokhrel S, Li N, Schoenfeld D, Meng H, Lin S, Wang X, Wang M, Ji Z, Zink JI, Mädler L, Castranova V, Lin S, Nel AE. Decreased Dissolution of ZnO by Iron Doping Yields Nanoparticles with Reduced Toxicity in the Rodent Lung and Zebrafish Embryos. ACS Nano. 2011; 5:1223–1235. [PubMed: 21250651]
24. Zhang H, Ji Z, Xia T, Meng H, Low-Kam C, Liu R, Pokhrel S, Lin S, Wang X, Liao YP, Wang M, Li L, Rallo R, Damoiseaux R, Telesca D, Mädler L, Cohen Y, Zink JI, Nel AE. Use of Metal Oxide Nanoparticle Band Gap To Develop a Predictive Paradigm for Oxidative Stress and A cute Pulmonary Inflammation. ACS Nano. 2012; 6:4349–4368. [PubMed: 22502734]
25. Karlsson HL, Cronholm P, Gustafsson J, Möller L. Copper Oxide Nanoparticles Are Highly Toxic: A Comparison Between Metal Oxide Nanoparticles and Carbon Nanotubes. Chem Res Toxicol. 2008; 21:1726–1732. [PubMed: 18710264]
26. Limbach LK, Wick P, Manser P, Grass RN, Bruinink A, Stark WJ. Exposure of Engineered Nanoparticles to Human Lung Epithelial Cells: Influence of Chemical Composition and Catalytic Activity on Oxidative Stress. Environ Sci Technol. 2007; 41:4158–4163. [PubMed: 17612205]
27. Bondarenko O, Ivask A, Käkinen A, Kahru A. Sub-Toxic Effects of CuO Nanoparticles on Bacteria: Kinetics, Role of Cu Ions and Possible Mechanisms of Action. Environ Pollut. 2012; 169:81–89. [PubMed: 22694973]
28. Chang YN, Zhang M, Xia L, Zhang J, Xing G. The Toxic Effects and Mechanisms of CuO and ZnO Nanoparticles. Mater. 2012; 5:2850–2871.
29. Toduka Y, Toyooka T, Ibuki Y. Flow Cytometric Evaluation of Nanoparticles Using Side-Scattered Light and Reactive Oxygen Species-Mediated Fluorescence–Correlation with Genotoxicity. Environ Sci Technol. 2012; 46:7629–7636. [PubMed: 22703531]
30. Khachatryan L, Vejerano E, Lomnicki S, Dellinger B. Environmentally Persistent Free Radicals (EPFRs). 1. Generation of Reactive Oxygen Species in Aqueous Solutions. Environ Sci Technol. 2011; 45:8559–8566. [PubMed: 21823585]
31. Moschini E, Gualtieri M, Colombo M, Fascio U, Camatini M, Mantecca P. The Modality of Cell–Particle Interactions Drives the Toxicity of Nanosized CuO and TiO_2 in Human Alveolar Epithelial Cells. Toxicol Lett. 2013; 222:102–116. [PubMed: 23906720]
32. Muller EB, Lin S, Nisbet RM. Quantitative Adverse Outcome Pathway Analysis of Hatching in Zebrafish with CuO Nanoparticles. Environ Sci Technol. 2015; 49:11817–11824. [PubMed: 26378804]
33. Pham ALT, Doyle FM, Sedlak DL. Kinetics and Efficiency of H_2O_2 Activation by Iron-Containing Minerals and Aquifer Materials. Water Res. 2012; 46:6454–6462. [PubMed: 23047055]

34. Twickler M, Dallinga-Thie G, Cramer MJ. Trojan Horse Hypothesis: Inhaled Airborne Particles, Lipid Bullets, and Atherogenesis. JAMA. 2006; 295:2354–2355. [PubMed: 16720818]
35. Grosell, M. 2- Copper. In: Chris, M.Wood, APF., Colin, JB., editors. Fish Physiol. Vol. 31. Academic Press; 2011. p. 53-133.
36. An L, Liu S, Yang Z, Zhang T. Cognitive Impairment in Rats Induced by Nano-CuO and Its Possible Mechanisms. Toxicol Lett. 2012; 213:220–227. [PubMed: 22820425]
37. Bulcke F, Santofimia-Castaño P, Gonzalez-Mateos A, Dringen R. Modulation of Copper Accumulation and Copper-Induced Toxicity by Antioxidants and Copper Chelators in Cultured Primary Brain Astrocytes. J Trace Elem Med Biol. 2015; 32:168–176. [PubMed: 26302925]
38. Ahamed M, Akhtar MJ, Alhadlaq HA, Alrokayan SA. Assessment of the Lung Toxicity of Copper Oxide Nanoparticles: Current Status. Nanomedicine. 2015; 10:2365–2377. [PubMed: 26251192]
39. Kuschner WG, D'Alessandro A, Hambleton J, Blanc PD. Tumor Necrosis Factor-Alpha and Interleukin-8 Release from U937 Human Mononuclear Cells Exposed to Zinc Oxide *in Vitro*: Mechanistic Implications for Metal Fume Fever. J Occup Env Med. 1998; 40:454–459. [PubMed: 9604183]
40. Li R, Ji Z, Qin H, Kang X, Sun B, Wang M, Chang CH, Wang X, Zhang H, Zou H, Nel AE, Xia T. Interference in Autophagosome Fusion by Rare Earth Nanoparticles Disrupts Autophagic Flux and Regulation of an Interleukin-1β Producing Inflammasome. ACS Nano. 2014; 8:10280–10292. [PubMed: 25251502]
41. U.S. EPA. Lead and Copper Rule: A Quick Reference Guide. Washington, DC: 2004. Vol. EPA 816-F-04-009
42. Ivask A, Titma T, Visnapuu M, Vija H, Kakinen A, Sihtmae M, Pokhrel S, Mädler L, Heinlaan M, Kisand V, Shimmo R, Kahru A. Toxicity of 11 Metal Oxide Nanoparticles to Three Mammalian Cell Types. In Vitro Curr Trends Med Chem. 2015; 15:1914–1929.
43. Torres-Duarte C, Adeleye AS, Pokhrel S, Mädler L, Keller AA, Cherr GN. Developmental Effects of Two Different Copper Oxide Nanomaterials in Sea Urchin (*Lytechinus Pictus*) Embryos. Nanotoxicology. 2015; 10:1–9.
44. Youngsik S, Young-Sik C, Young-Duk H, Heonyong P. Copper Ion from Cu_2O Crystal Induces AMPK-Mediated Autophagy *via* Superoxide in Endothelial Cells. Mol Cells. 2016; 39:195–203. [PubMed: 26743904]
45. Fairbairn EA, Keller AA, Mädler L, Zhou D, Pokhrel S, Cherr GN. Metal Oxide Nanomaterials in Seawater: Linking Physicochemical Characteristics with Biological Response in Sea Urchin Development. J Hazard Mater. 2011; 192:1565–1571. [PubMed: 21775060]
46. George S, Pokhrel S, Xia T, Gilbert B, Ji Z, Schowalter M, Rosenauer A, Damoiseaux R, Bradley KA, Mädler L, Nel AE. Use of a Rapid Cytotoxicity Screening Approach To Engineer a Safer Zinc Oxide Nanoparticle Through Iron Doping. ACS Nano. 2010; 4:15–29. [PubMed: 20043640]
47. Peralta G, Puggioni D, Filippetti A, Fiorentini V. Jahn-Teller Stabilization of Magnetic and Orbital Ordering in Rocksalt CuO. Phys Rev B. 2009; 80:140408.
48. Tyurin AG. On the Nature of the Effect of Copper on the Corrosion Resistance of Iron. Prot Met. 2004; 40:232–239.
49. Pokhrel S, Birkenstock J, Schowalter M, Rosenauer A, Mädler L. Growth of Ultrafine Single Crystalline WO_3 Nanoparticles Using Flame Spray Pyrolysis. Cryst Growth Des. 2010; 10:632–639.
50. Teoh WY, Amal R, Mädler L. Flame Spray Pyrolysis: An Enabling Technology for Nanoparticles Design and Fabrication. Nanoscale. 2010; 2:1324–1347. [PubMed: 20820719]
51. Darakchieva V, Beckers M, Xie MY, Hultman L, Monemar B, Carlin JF, Feltin E, Gonschorek M, Grandjean N. Effects of Strain and Composition on the Lattice Parameters and Applicability of Vegard's Rule in Al-Rich $Al_{1-x}In_xN$ Films Grown on Sapphire. J Appl Phys. 2008; 103:103513.
52. Asbrink S, Waskowska A. CuO: X-Ray Single-Crystal Structure Determination at 196 K and Room Temperature. J Phys : Condens Matter. 1991; 3:8173.
53. Sarma DD, Sreedhar K. Electronic Structure of Square Planar CuO_4^{6-}Clusters. Z Physik B-Condensed Matter. 1988; 69:529–534.
54. Shannon RD. Revised Effective Ionic Radii and Systematic Studies of Interatomic Distances in Halides and Chalcogenides. Acta Crystallogr Sect A. 1976; 32:751–767.

55. Attfield JP, Kharlanov AL, McAllister JA. Cation Effects in Doped La_2CuO_4 Superconductors. Nature. 1998; 394:157–159.
56. Moskvin AS, Loshkareva NNYPS, Yu P, Sidorov MA, Samokhvalov AA. Characteristic Features of the Electronic Structure of Copper Oxide (CuO): Initiation of the Polar Configuration Phase and Middle-IR Optical Absorption. Zh Eksp Teor Fiz. 1993; 105:967–993.
57. Bocher L, Popova E, Nolan M, Gloter A, Chikoidze E, March K, Warot-Fonrose B, Berini B, Stéphan O, Keller N, Dumont Y. Direct Evidence of Fe^{2+}-Fe^{3+} Charge Ordering in the Ferrimagnetic Hematite-Ilmenite $Fe_{1.35}Ti_{0.65}O_{3-d}$ Thin Films. Phys Rev Lett. 2013; 111:167202. [PubMed: 24182295]
58. Garvie LAJ, Craven AJ, Brydson R. Use of Electron-Energy Loss Near-Edge Fine Structure in the Study of Minerals. Am Mineral. 1994; 79:411–425.
59. Chrzanowski J, Irwin JC. Raman Scattering from Cupric Oxide. Solid State Commun. 1989; 70:11–14.
60. Xu JF, Ji W, Shen ZX, Li WS, Tang SH, Ye XR, Jia DZ, Xin XQ. Raman Spectra of CuO Nanocrystals. J Raman Spectrosc. 1999; 30:413–415.
61. Chapelle A, Barnabé A, Presmanes L, Tailhades P. Copper and Iron Based Thin Film Nanocomposites Prepared by Radio-Frequency Sputtering. Part II: Elaboration and Characterization of Oxide/Oxide Thin Film Nanocomposites Using Controlled *Ex-Situ* Oxidation Process. J Mater Sci. 2013; 48:3304–3314.
62. George S, Pokhrel S, Ji Z, Henderson BL, Xia T, Li L, Zink JI, Nel AE, Mädler L. Role of Fe Doping in Tuning the Band Gap of TiO_2 for the Photo-Oxidation-Induced Cytotoxicity Paradigm. J Am Chem Soc. 2011; 133:11270–11278. [PubMed: 21678906]
63. Cressey G, Henderson CMB, van der Laan G. Use of *L*-Edge X-Ray Absorption Spectroscopy to Characterize Multiple Valence States of 3*d* Transition Metals; A New Probe for Mineralogical and Geochemical Research. Phys Chem Miner. 1993; 20:111–119.
64. Krishnan KM. Iron L $_{3,2}$ Near-Edge Fine Structure Studies. Ultramicroscopy. 1990; 32:309–311.
65. Joseph DP, Venkateswaran C, Vennila RS. Critical Analysis on the Structural and Magnetic Properties of Bulk and Nanocrystalline Cu-Fe-O. Adv Mater Sci Eng. 2010; 2010:1–14.
66. Atia TA, Altimari P, Moscardini E, Pettiti I, Toro L, Pagnanelli F. Synthesis and Characterization of Copper Ferrite Magnetic Nanoparticles by Hydrothermal Route. Chem Eng Trans. 2016; 47:151–156.
67. Hashemian S. Kinetic and Thermodynamic of Adsorption of Methylene Blue (MB) by $CuFe_2O_4$/Rice Bran Composite. Int J Phys Sci. 2011; 6:6257–6267.
68. Delgado AG, Parameswaran P, Fajardo-Williams D, Halden RU, Krajmalnik-Brown R. Role of Bicarbonate as a pH Buffer and Electron Sink in Microbial Dechlorination of Chloroethenes. Microb Cell Fact. 2012; 11:1–11. [PubMed: 22214286]
69. Deng Y, Handoko DA, Du Y, Xi S, Yeo SB. *In Situ* Raman Spectroscopy of Copper and Copper Oxide Surfaces During Electrochemical Oxygen Evolution Reaction: Identi cation of Cu^{III}Oxides as Catalytically Active Species. ACS Catal. 2016; 6:2473–2481.
70. Jayalakshmi M, Balasubramanian K. Cyclic Voltammetric Behavior of Copper Powder Immobilized on Paraffin Impregnated Graphite Electrode in Dilute Alkali Solution. Int J Electrochem Sci. 2008; 3:1277–1287.
71. Zhu M, Meng D, Wang C, Diao G. Facile Fabrication of Hierarchically Porous $CuFe_2O_4$ Nanospheres with Enhanced Capacitance Property. ACS Appl Mater Interfaces. 2013; 5:6030–6037. [PubMed: 23749233]
72. Sun T, Yan Y, Zhao Y, Guo F, Jiang C. Copper Oxide Nanoparticles Induce Autophagic Cell Death in A549 Cells. PLoS ONE. 2012; 7:e43442. [PubMed: 22916263]
73. Thit A, Selck H, Bjerregaard HF. Toxic Mechanisms of Copper Oxide Nanoparticles in Epithelial Kidney Cells. Toxicol In Vitro. 2015; 29:1053–1059. [PubMed: 25862124]
74. Aruoja V, Dubourguier HC, Kasemets K, Kahru A. Toxicity of Nanoparticles of CuO, ZnO and TiO_2 to Microalgae *Pseudokirchneriella Subcapitata*. Sci Total Environ. 2009; 407:1461–1468. [PubMed: 19038417]
75. Bao S, Lu Q, Fang T, Dai H, Zhang C. An Assessment of the Toxicity of CuO Nanoparticles Using Multiple-Gene-Deleted Mutants of *Saccharomyces Cerevisiae*. Appl Environ Microbiol. 2015

76. Hedberg J, Karlsson HL, Hedberg Y, Blomberg E, Odnevall Wallinder I. The Importance of Extracellular Speciation and Corrosion of Copper Nanoparticles on Lung Cell Membrane Integrity. Colloids Surf, B. 2016; 141:291–300.
77. Lever, ABP. Inorganic Electronic Spectroscopy. Amsterdam: Elsevier Pub. Co; 1968.
78. Cotton, FA., Wilkinson, G., Murrillo, CA., Bochmann, M. Advanced Inorganic Chemistry. 6. John Wiley & Sons, Inc; 1999.
79. Faungnawakij K, Shimoda N, Fukunaga T, Kikuchi R, Eguchi K. Crystal Structure and Surface Species of $CuFe_2O_4$ Spinel Catalysts in Steam Reforming of Dimethyl Ether. Appl Catal, B. 2009; 92:341–350.
80. Nedkov I, Vandenberghe RE, Marinova T, Thailhades P, Merodiiska T, Avramova I. Magnetic Structure and Collective Jahn–Teller Distortions in Nanostructured Particles of $CuFe_2O_4$. Appl Surf Sci. 2006; 253:2589–2596.
81. Aruoja V, Pokhrel S, Sihtmae M, Mortimer M, Mädler L, Kahru A. Toxicity of 12 Metal-Based Nanoparticles to Algae, Bacteria and Protozoa. Environ Sci: Nano. 2015; 2:630–644.
82. Kahru A, Dubourguier HC. From Ecotoxicology to Nanoecotoxicology. Toxicology. 2010; 269:105–19. [PubMed: 19732804]
83. Kemmler JA, Pokhrel S, Mädler L, Weimar U, Barsan N. Flame Spray Pyrolysis for Sensing at the Nanoscale. Nanotechnology. 2013; 24:442001. [PubMed: 24113649]
84. Mukherjee A, Pokhrel S, Bandyopadhyay S, Mädler L, Peralta-Videa JR, Gardea-Torresdey JL. A Soil Mediated Phyto-Toxicological Study of Iron Doped Zinc Oxide Nanoparticles (Fe@ZnO) in Green Peas (*Pisum sativum L.*). Chem Eng J. 2014; 258:394–401.
85. Xiao J, Kuc A, Pokhrel S, Mädler L, Pöttgen R, Winter F, Frauenheim T, Heine T. Fe-Doped ZnO Nanoparticles: The Oxidation Number and Local Charge on Iron, Studied by 57Fe Mößbauer Spectroscopy and DFT Calculations. Chem -Eur J. 2013; 19:3287–3291. [PubMed: 23400908]
86. Xiao J, Kuc A, Pokhrel S, Schowalter M, Parlapalli S, Rosenauer A, Frauenheim T, Mädler L, Pettersson LGM, Heine T. Evidence for Fe^{2+} in Wurtzite Coordination: Iron Doping Stabilizes ZnO Nanoparticles. Small. 2011; 7:2879–2886. [PubMed: 21913325]
87. Gilbert B, Fakra SC, Xia T, Pokhrel S, Mädler L, Nel AE. The Fate of ZnO Nanoparticles Administered to Human Bronchial Epithelial Cells. ACS Nano. 2012; 6:4921–4930. [PubMed: 22646753]
88. Minnermann M, Pokhrel S, Thiel K, Henkel R, Birkenstock J, Laurus T, Zargham A, Flege JI, Zielasek V, Piskorska-Hommel E, Falta J, Mädler L, Bäumer M. Role of Palladium in Iron Based Fischer Tropsch Catalysts Prepared by Flame Spray Pyrolysis. J Phys Chem C. 2011; 115:1302–1310.
89. Kemmler JA, Pokhrel S, Birkenstock J, Schowalter M, Rosenauer A, Bârsan N, Weimar U, Mädler L. Quenched, Nanocrystalline $In_4Sn_3O_{12}$ High Temperature Phase for Gas Sensing Applications. Sens Actuators, B. 2012; 161:740–747.
90. Birkenstock J, Fischer RX, Messner T. The Bremen Rietveld Analysis and Structure Suite. BRASS. 2009
91. Hill RJ, Fischer RX. Profile Agreement Indices in Rietveld and Pattern-Fitting Analysis. J Appl Crystallogr. 1990; 23:462–468.
92. Zhang H, Pokhrel S, Ji Z, Meng H, Wang X, Lin S, Chang CH, Li L, Li R, Sun B, Wang M, Liao YP, Liu R, Xia T, Mädler L, Nel AE. PdO Doping Tunes Band-Gap Energy Levels as Well as Oxidative Stress Responses to a Co_3O_4 p-Type Semiconductor in Cells and the Lung. J Am Chem Soc. 2014; 136:6406–6420. [PubMed: 24673286]
93. Schopf SO, Salameh S, Mädler L. Transfer of Highly Porous Nanoparticle Layers to Various Substrates Through Mechanical Compression. Nanoscale. 2013; 5:3764–3772. [PubMed: 23532446]

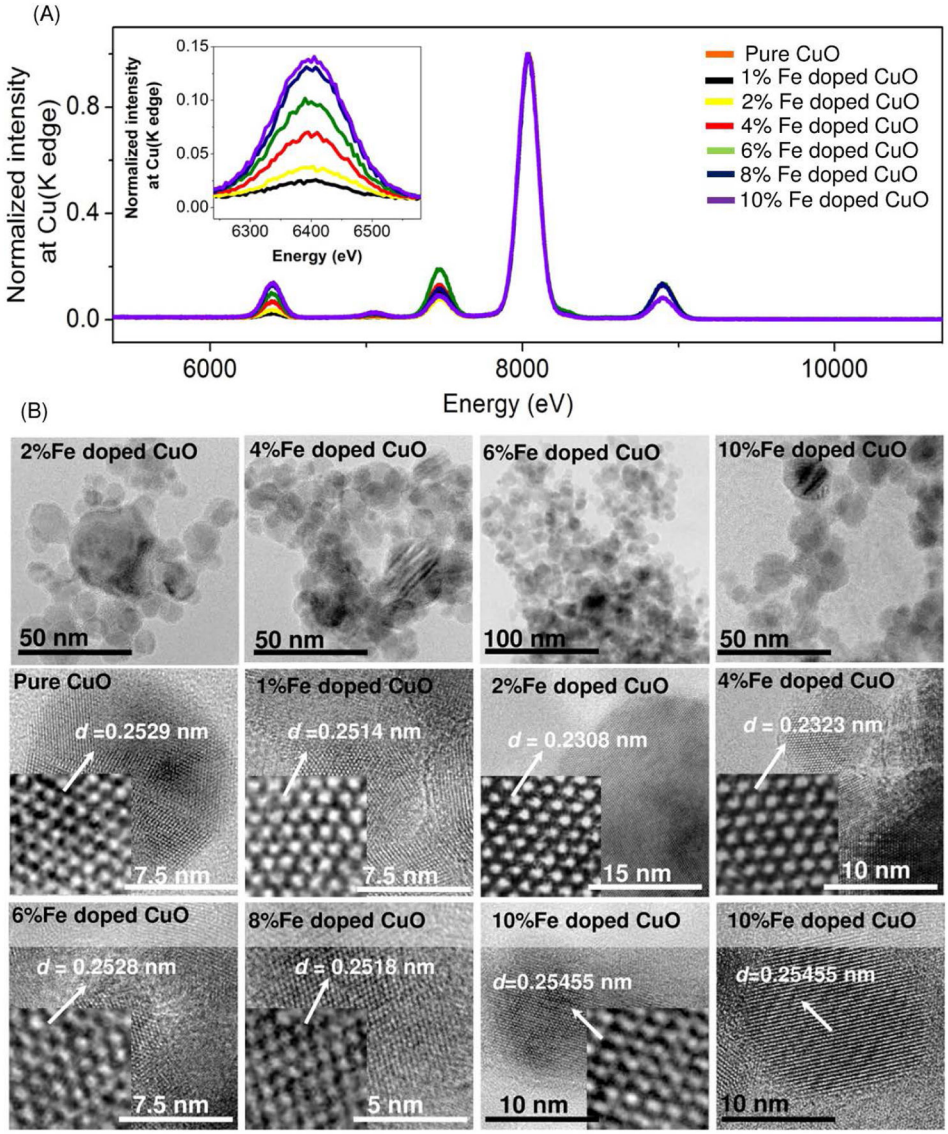

Figure 1.

(A) EDX analyses of the Fe doped CuO NPs. The results show good agreement with the Fe loading during FSP and the amount of Fe present in each sample. (B) Overview and high resolution TEM images of pure and Fe doped CuO NPs.

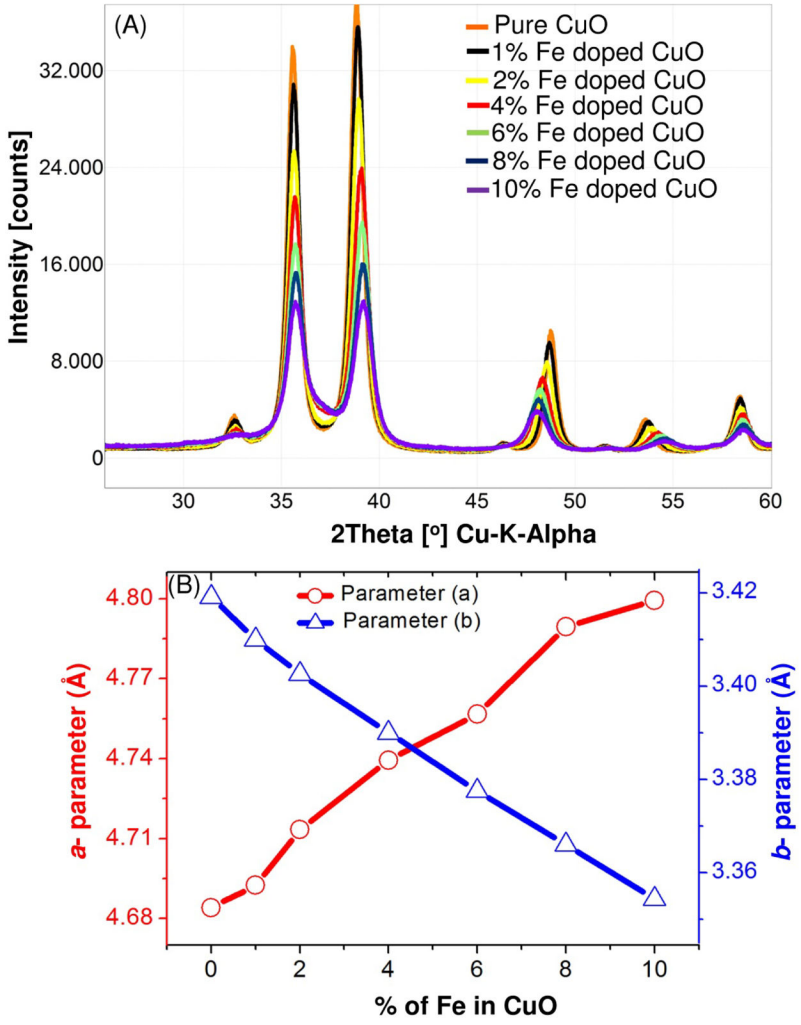

Figure 2.

(A) XRD patterns of Fe doped CuO. The shift in the patterns at different 2θ angles shows Fe incorporation within the CuO lattice. The lower XRD intensity with increasing Fe doping supports such incorporation. (B) The a parameter of the CuO crystal structure consistently increases while the b parameter decreases with increased Fedoping.

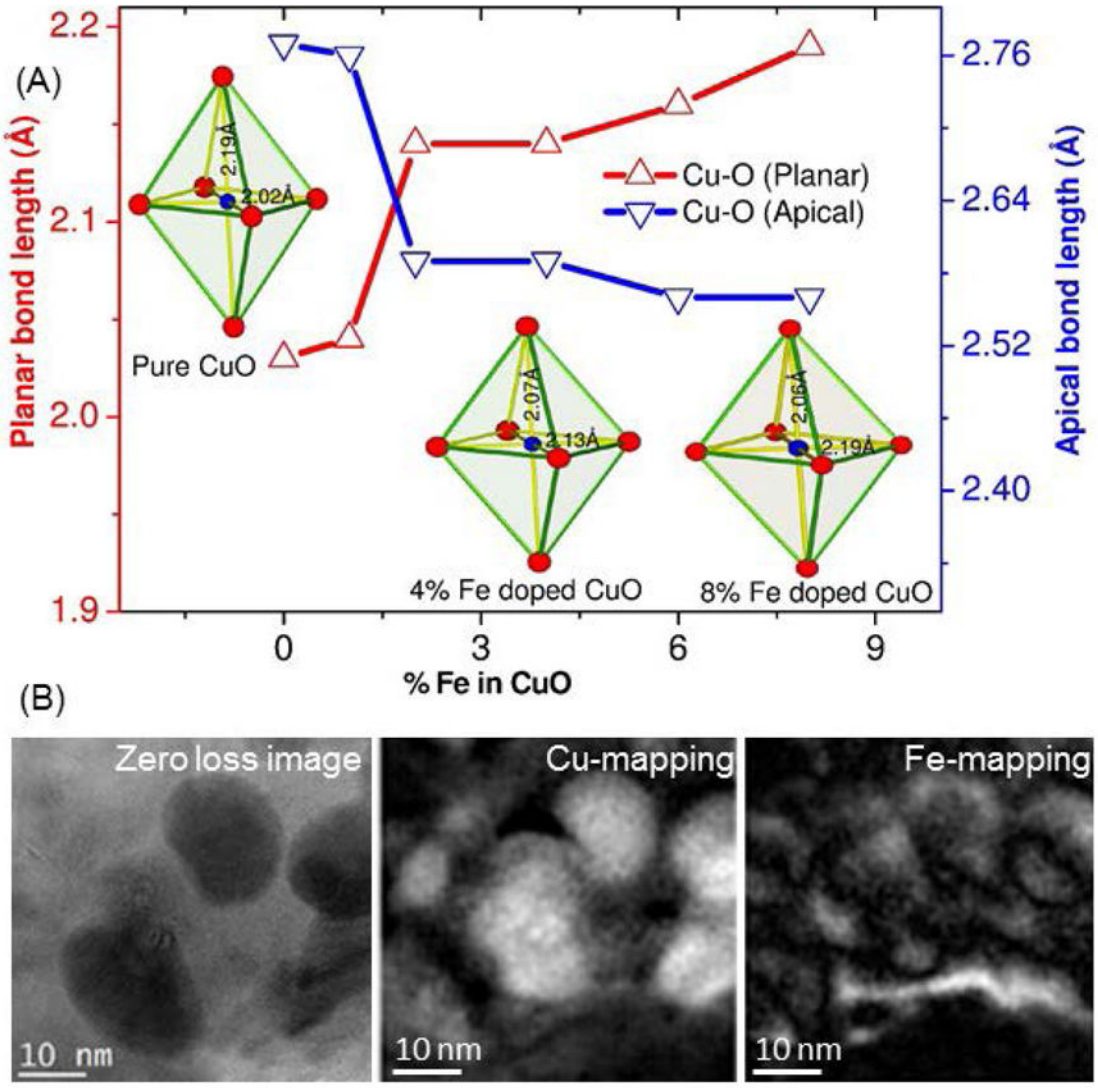

Figure 3.

(A) The structural analyses of Fe doped CuO NPs. The increase in planar Cu-O and decrease in apical Cu-O bond length between 2% and 4% Fe doping shows strong distortion of the octahedra and after 4% such distortion is rather slow. The results show Fe is incorporated in CuO with lattice distortion of almost 4.1 % at higher Fe doping. (B) The energy filtered transmission electron microscopy of 10% Fe doped CuO NPs: (left panel) zero loss image of the experimental probe, (middle panel) image of the Cu mapping and (right panel) image of the Fe mapping of the Fe doped CuO NPs distribution. The results show homogeneous distribution of the Fe in CuO NPs.

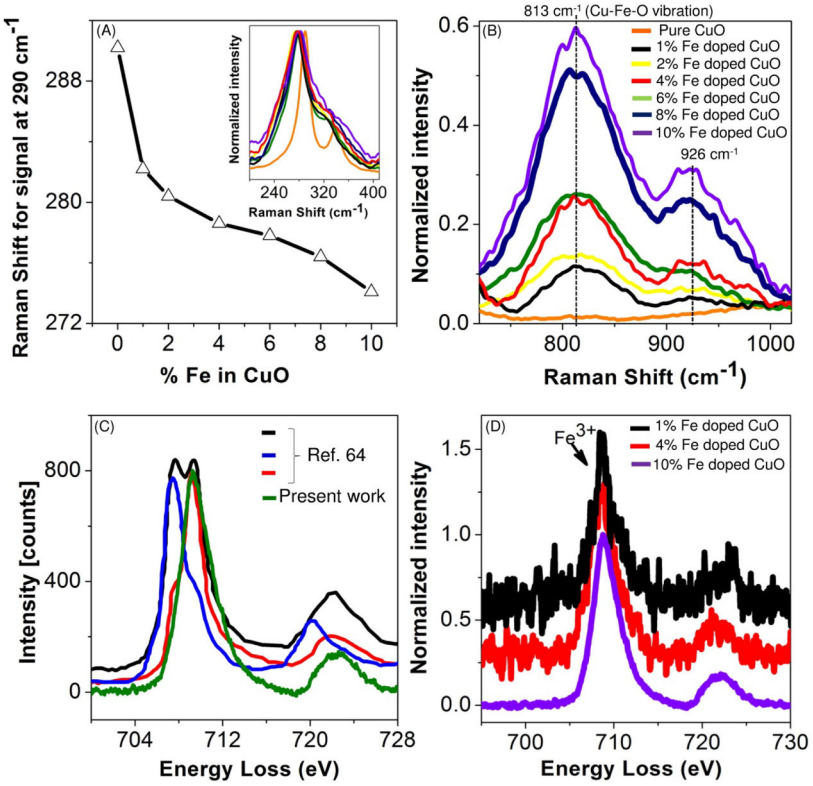

Figure 4.

(A) Room temperature Raman shift at 291 cm^{-1} of CuO with Fe doping. (B) Increasing intensity of Raman signals at 813 and 926 cm^{-1} are assigned to ν(Cu-Fe-O). (C) Black, red and blue EELS signals of Fe^{2+}/Fe^{3+} are adapted from the literature [57–58] while the green pattern was measured for 10% Fe doped CuO NPs. (D) The comparison of the EELS spectra occurring at 708.8 eV for 1, 4 and 10% Fe doped CuO demonstrating Fe^{3+}oxidation state for all the dopings.

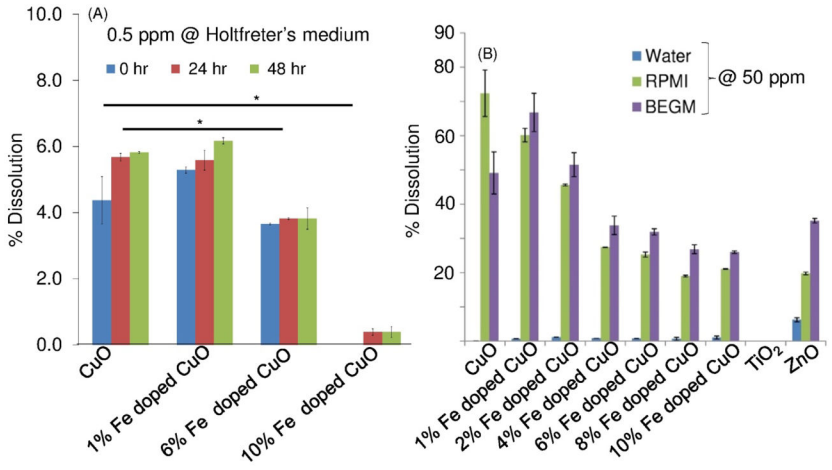

Figure 5.

The experimental results of Cu^{2+} release from 0–10% Fe doped CuO NPs. (A) Dissolution profile of Fe doped CuO in Holtfreter's medium at 0.5 ppm. The dissolution profile shows Cu^{2+} release is significantly reduced via Fe doping. (B) The release data in RPMI and BEGM cell medium exposed to 50 ppm of NPs show consistent decrease in the Cu^{2+} release while in pure water the dissolution is not significant.

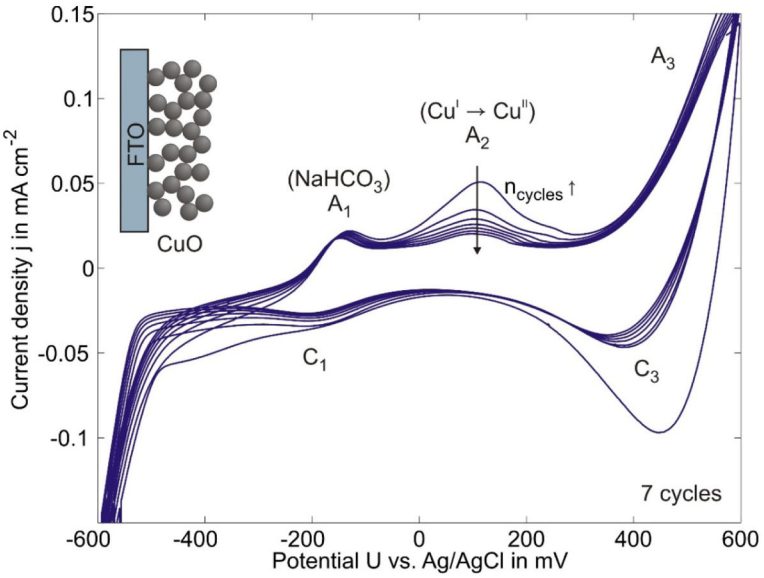

Figure 6.

CV of pure CuO in Holtfreter's solution recorded at 25 mVs^{-1}. The pure CuO showed two anodic peaks, A_1 is related to the corresponding cathodic signal C_1 indicating redox reaction with the carbonate species and A_2 corresponds to Cu^{+}/Cu^{2+} redox couple with the reduction occurring below −400 mV.

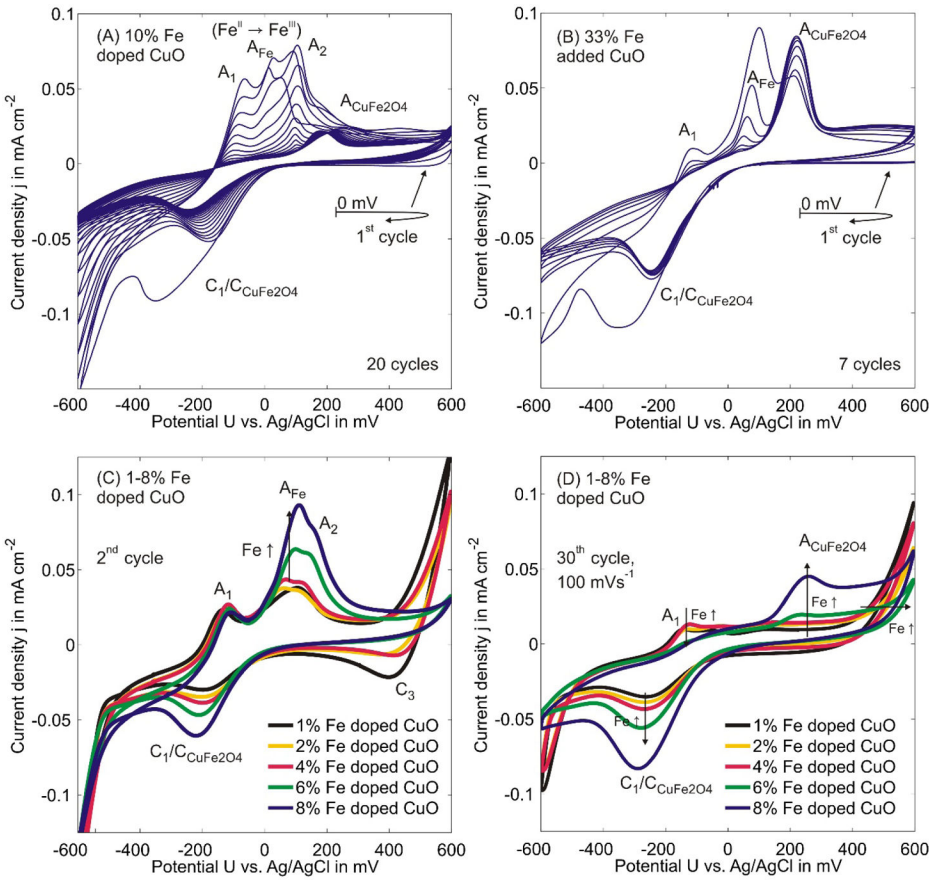

Figure 7.

Cyclic voltammetry of (A) 10% Fe doped CuO, (B) 33% Fe added CuO, 1–8%Fe doped CuO (only 2nd cycle) recorded at 25 mVs^{-1} and (D) 1–8% Fe doped CuO (30th cycle) recorded at 100 mVs^{-1}. While two new signals $A_{CuFe2O4}$ and $C_{CuFe2O4}$ were observed for 10% Fe doped CuO, their intensities were highest for 33% Fe doped CuO due to $CuFe_2O_4$. The quasi-stationary 30th cycles shows the spinel $CuFe_2O_4$ formation at the surface and decreasing oxidation of CuO involving sodium bicarbonate (A_1 signal) with increasing Fe.

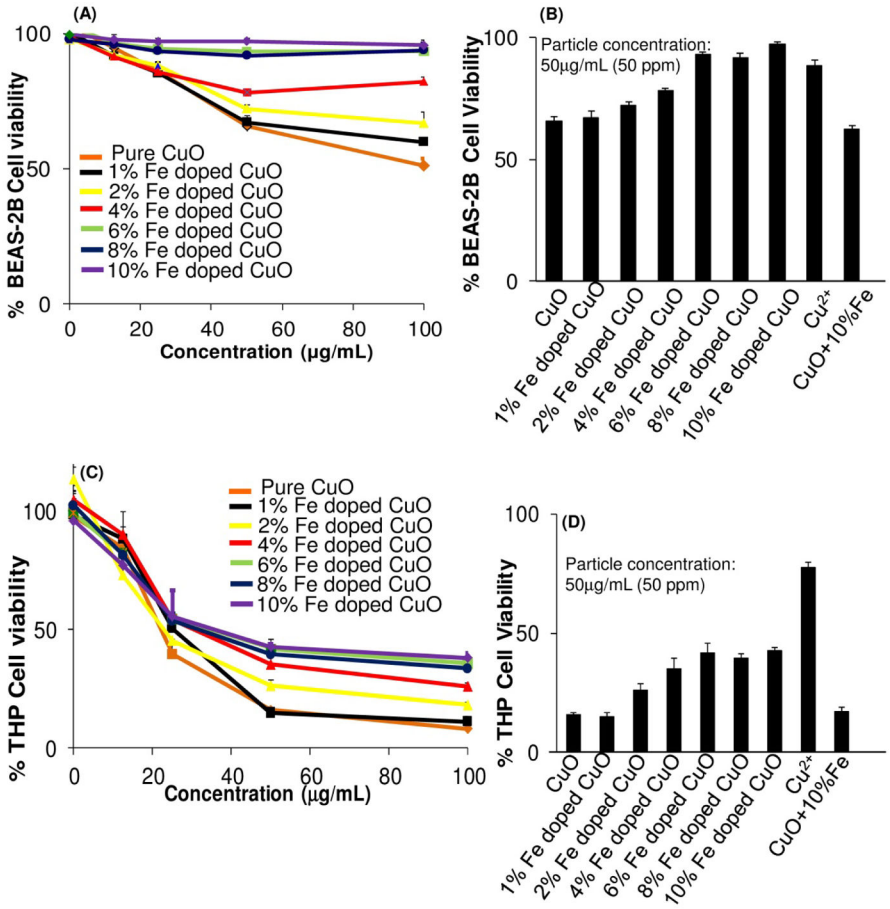

Figure 8.

Iron doping reduced the toxicity of CuO NPs in BEAS-2B (panels A and B)) and THP-1 cells (panels C and D). BEAS-2B or THP-1 cells were incubated with 0–100 µg/mL (0–100 ppm) (A and C) or 50 µg/mL (B and D) pure or doped CuO NPs for 24 h. The cell viability was determined by MTS assay exposed to 50 µg/mL (50 ppm) of NPs.

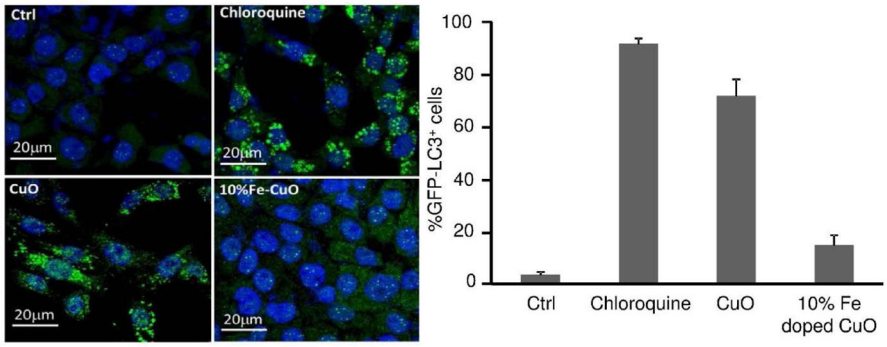

Figure 9.

(left panel) Accumulation of autophagosomes as determined by fluorescent staining with FITC-labeled anti-LC-3II. The images show extensive autophasosome induction by 50 ppm chloroquin (CQ) as a result of its effects of interfering in autophagic flux. CuO had the same effect on autophagosome accumulation, which disappeared for 10% Fe doped CuO (50 ppm). (right panel) Quantification of the Cu^{2+} by exposing CuO and 10%Fe doped CuO in the cells.

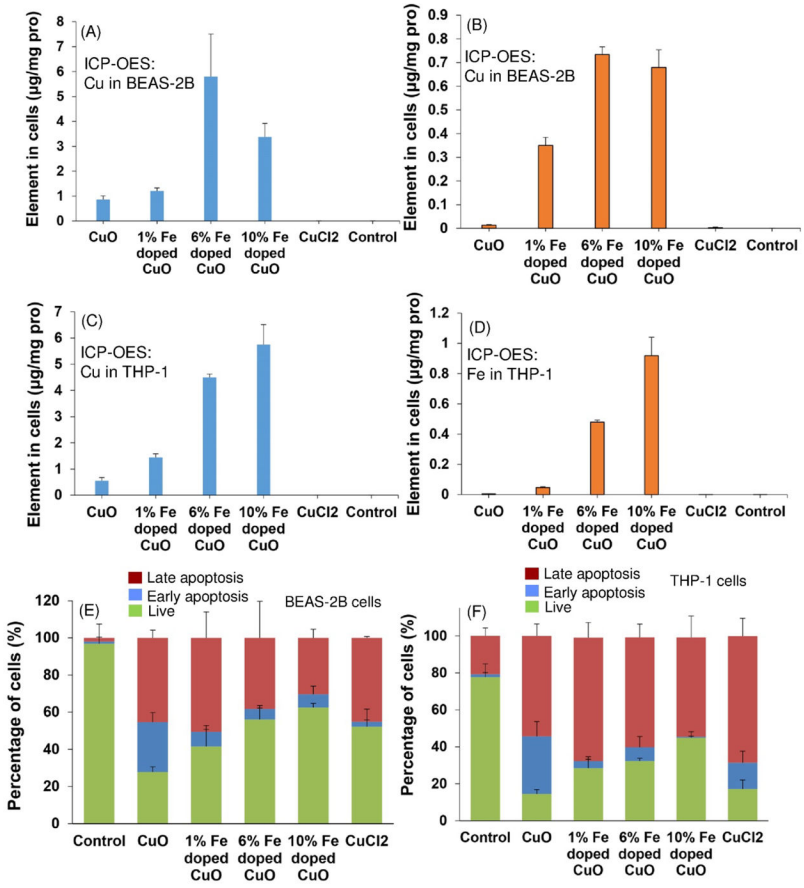

Figure 10.

(A)–(D) The quantification of Cu and Fe in BEAS-2B and THP-1 cells using ICP-OES after incubating with 0–10% Fe doped CuO NPs and $CuCl_2$ (control) for 24 h at 50 ppm. (E)–(F) Results of the early apoptosis, late apoptosis/necrosis, and live BEAS-2B and THP-1 cells demonstrating effective reduction of apoptosis via Fe doping.

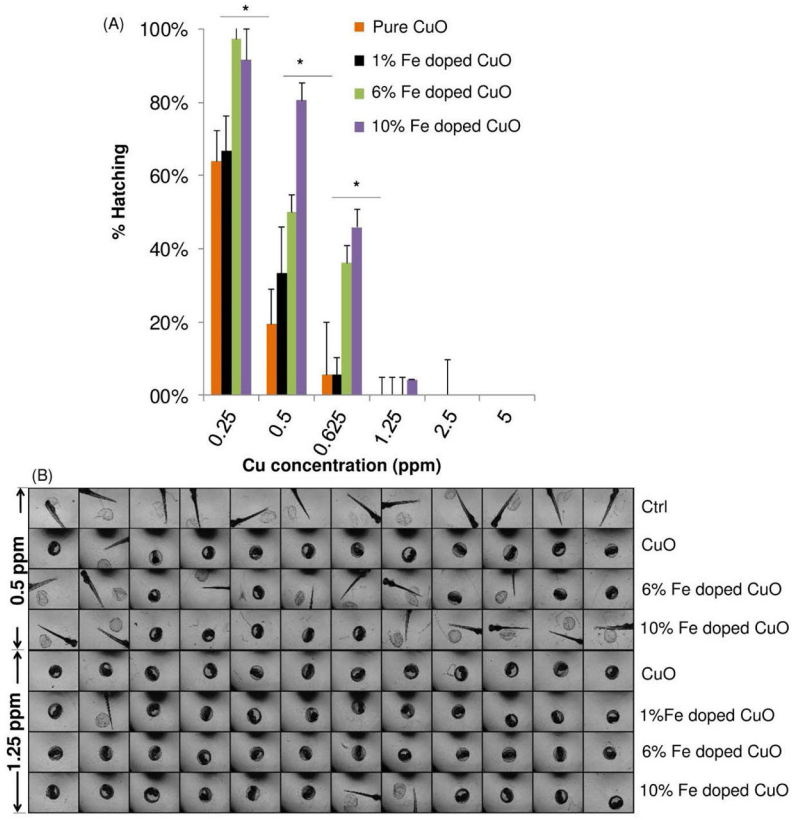

Figure 11.

(A) Dose-dependent effects of non-doped and doped (1%, 6% and 10% Fe) CuO on zebrafish embryo hatching (%). Embryo hatching was studied in 96 well plates with automated high content imaging, demonstrating progressive hatching interference by CuO at doses ≥ 0.25 ppm. While Fe doping lead to reduced hatching interference at 0.25, 0.5 and 0.625 ppm CuO, the doping effect disappeared at a nanoparticle concentration ≥1.25 ppm. (B) Representative light optic images obtained in the experiment.

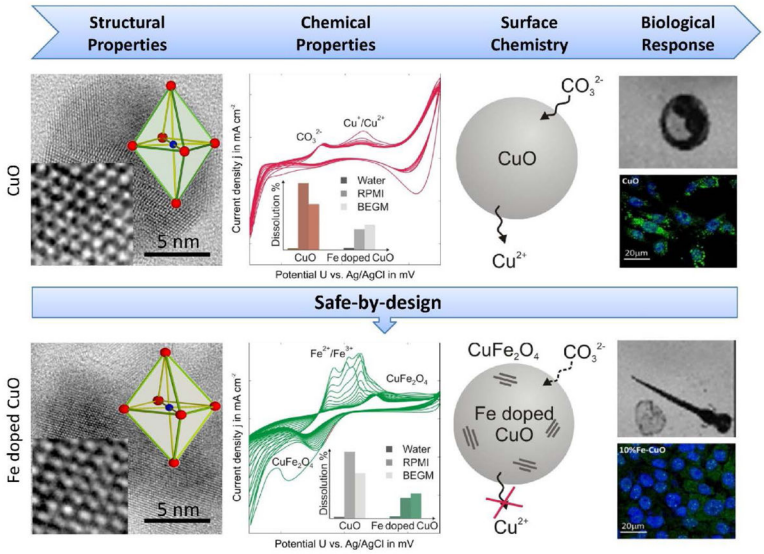

Figure 12.

Structural-activity-relationship describing the structural and chemical properties of pure and Fe doped CuO NPs and their influence to the biological response assessment.

Table 1

Specific surface area, primary particle size, hydrodynamic size of pure and Fe doped CuO NPs.

Properties/Materials	CuO	1%Fe-CuO	2%Fe-CuO	4%Fe-CuO	6%Fe-CuO	8%Fe-CuO	10%Fe-CuO
Specific surface area (m2/g), primary particle sizes (nm) and crystallite sizes (nm)							
SSA (m^2/g)	80.9 (±2.5)	79.2 (±3.2)	77.6 (±1.8)	89.6 (±4.2)	92.9 (±3.6)	93.6 (±4.5)	90.4 (±1.2)
d_{BET} (nm)	11.8 (±1.3)	12.0 (±1.5)	12.3 (±1.2)	10.7 (±1.8)	10.3 (±1.6)	10.3 (±1.9)	10.7 (±1.0)
d_{XRD} (nm)	9.4 (±0.1)	11.9 (±0.4)	9.2 (±0.1)	10.5 (±0.1)	10.8 (±0.1)	9.8 (±0.4)	9.6 (±0.9)
Hydrodynamic sizes (nm)							
DI water (pH~7)	210 ± 6	284 ± 11	287 ± 2	312 ± 5	270 ± 1	318 ± 8	434 ± 12
Holfreters Medium (pH~7.6)	264.9±7.1	279.3±4.2	456.7±3.0	423.1±9.6	381.4±14.6	450.6±7.1	224.9±3.2
RPMI 1640 medium (pH~7.6)	394 ± 29	388 ± 16	375 ± 12	664 ± 42	388 ± 25	366 ± 12	349 ± 48
BEGM medium (pH~7.6)	366 ± 1	520 ± 59	474 ± 4	477 ± 36	467 ± 48	638 ± 36	546 ± 17
Zetapotential (ξ) mV							
DI H_2O (pH~7)	41.5 ± 0.8	38.1 ± 0.4	38.4 ± 0.9	37.2 ± 1.1	32.6 ± 3.0	−14.9 ± 3.0	−21.6 ± 0.5
Holfreters Medium (pH~7.6)	−12.63±0.95	−22.74±4.49	−23.16±5.81	−17.63±1.7	−22.58±3.1	−19.41±0.8	−16.45±3.2
RPMI 1640 medium (pH~7.6)	−16.6 ± 1.0	−8.5 ± 2.9	−11.1 ± 2.5	−9.8 ± 3.0	−9.4 ± 0.4	−9.4 ± 2.9	−17.2 ± 4.2
BEGM medium (pH~7.6)	−15.6 ± 1.7	−16.5 ± 3.8	−11.3 ± 3.2	−20.3 ± 5.1	−19.2 ± 5.5	−10.2 ± 6.1	−13.4 ± 6.8
PdI							
DI H_2O	0.256	0.285	0.321	0.243	0.244	0.195	0.275
Holfreters Medium	0.261	0.182	0.272	0.254	0.206	0.25	0.113